ENGINEERING

Bioinspired growable humanoid robot with bone-mimetic linkages for versatile mobility

Hao Liu, Yanda Yang, Ting Wang, Jintao Yin, Hongqiang Wang*

Inspired by human biomechanics, humanoid robots are often designed to mimic human kinematics but typically lack key traits of developing bones, such as growability, lightweight yet stiff construction, and compliance for impact absorption. This work introduces a bone-inspired linkage structure with up to 315% extensibility, weighing only 350 grams while maintaining high load capacity, compliance, and stability. Integrated into a soft humanoid robot, these growable linkages enable dynamic shape adaptation, reducing height to 36% and width to 61%, to traverse tight spaces. By combining growable link actuation with servomotors, the robot switches to crawling mode and moves 1122 times faster than using motors or soft actuators alone. At just 4.5 kilograms, GrowHR can float, swim, walk on water, and fly. Its soft body ensures safe human interaction, allowing hugging, falling, and lifting without injury. Deformable legs demonstrate elastic energy storage and release under external loading, allowing motions beyond the limits of rigid structures. This work pioneers a growable, multifunctional robotic design approach for dynamic, complex environments.

INTRODUCTION

Humanoid robots, having humanlike appearance and capabilities, have the potential to perform diverse tasks and navigate terrains accessible to humans (*1*–*5*), making them a revolutionary technology for fields including healthcare (*6*–*8*), heavy labor (*9*, *10*), tele-existence (*11*, *12*), space exploration (*11*, *13*, *14*), and search and rescue operations particularly in hazardous environments (*12*, *15*–*17*). However, current robots still cannot be as good as humans in various aspects. For example, the bones of humans are made of multifunctional structures and complex components: The epiphyseal plate with osteoblasts grows the size of the bones with the nutrients from the arteries, the compact bones of high stiffness ensure the high load-bearing, the cancellous bone with spongy structure allows strong impact and mechanical connection with other structures, and the multiscale cavities in the marrow cavities and cancellous bones make the bone lightweight without sacrificing the stiffness (*18*). Despite that, current humanoid robots' frames are simple columns. Although growing robots are emerging in the last decades (*19*), they mainly mimic the combinations and interaction of molecules and cells (*20*). Recently, plant-inspired growing robots have achieved substantial progress (*21*, *22*). However, animal-inspired growable robots remain rare, as their locomotion must rely directly on the growing structures, which are required to bear dynamic loads, provide sufficient stiffness, and interact precisely with both the robot body and the environment. This demands that the growable mechanism be not only lightweight and multifunctional but also fast, efficient, and dimensionally accurate to maintain body balance and functional limb proportions during movement. Growable, walkable bipedal robots represent one of the most difficult challenges, owing to the inherent instability of bipedal walking.

Inspired by the structure of developing bones, the growable linkage integrates rigidity-flexibility coupling and multifunctional design. The soft chambers can expand up to 315% with air input, while the polyvinyl chloride (PVC) shell and cables with tension enable elastic energy storage (Fig. 1, A and B). A nonstretchable textile outer layer and linear guides provide high axial stiffness (up to 7.99 kN/m), and the two rigid adapters at each end facilitate mechanical connection. Moreover, a synchronous cable-constrained mechanism ensures that all cables extend uniformly during growth, keeping the upper and lower adapters parallel. The large internal chamber also contributes to lightweight construction, with the entire linkage weighing only 350 g. With the bone-inspired linkages, a growable humanoid robot (GrowHR) is implemented. It can increase its height by up to 278% (from 0.49 to 1.36 m, Fig. 1C) and walk at varying heights, by the carefully on-purpose designed structures and control algorithm for the stability and balance during standing and walking. This adaptability makes it suitable for compact package delivery and navigating through low openings (e.g., 0.55 m, 40.4% of the robot's full height) or narrow gaps (e.g., 0.25 m, 69.5% of the robot's full width) by deformation (Fig. 1D). Moreover, with the cooperation of the growing linkages and rigid servomotors, GrowHR crawls on the ground (112.2 mm/min), substantially outperforming locomotion powered by servomotors alone (0.1 mm/min). The big chamber of the growable linkages reduce the robot's weight to merely 4.5 kg (that was able to be lifted by a 6-year-old child in our demonstrations) and the density to only 5.8% of the water, allowing GrowHR to float (with a payload capacity 16.2 times its own weight), swim, walk on water, and even fly (assisted by additional ducted fans or quadrotors) to up 5.5 km away (Fig. 1D). Due to the adaptability and lightweight body, GrowHR is intrinsically safe for users, the environment, and itself, even when it bumps into surroundings or experiences strong impacts (with an acceleration of 599 m/s^2). We also demonstrated that the growable linkages could deform and store energy to deliver a powerful kick at a ball, a capability beyond the reach of rigid humanoid robots. This work establishes a foundation for the development of growable versatile humanoid robots that adapt to unstructured environment and enhance our daily lives in the future.

RESULTS

Design of growable linkage

Designing the linkages is challenging because they must be lightweight and capable of large, precise deformations, without unwanted deformation or tilting that interferes with standing and walking,

Department of Mechanical and Energy Engineering, Southern University of Science and Technology, Shenzhen, Guangdong 518055, China.
*Corresponding author. Email: wanghq6@sustech.edu.cn

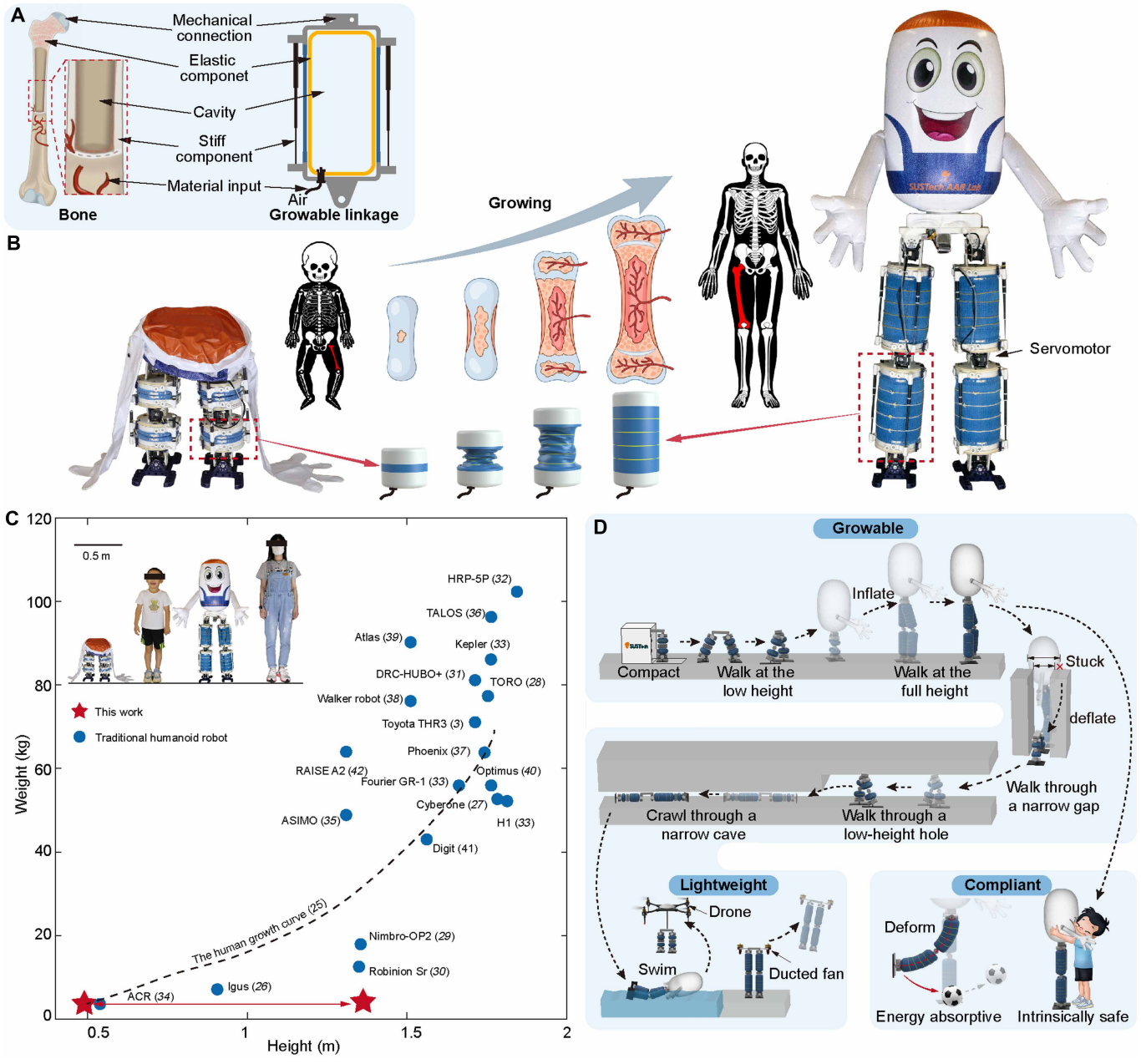

Fig. 1. The overview of GrowHR. (**A**) The structure of the growable linkage compared with bone. (**B**) Comparison between the growth mechanism of robots and the bone. (**C**) GrowHR's heights in the inflated and deflated states (represented by red stars), compared with a female adult (150 cm), a 6-year-old boy (115 cm), different robots (*3*, *26*–*42*), and the human growth curve (*25*). (**D**) Application scenarios of GrowHR.

while also being sufficiently stiff to support the robot's body. These are typically conflicting requirements, as noted in previous soft robotics research (*23*, *24*). Inspired by the developing bones, we designed the growable linkage with soft layers made from PVC material for deformation after inflation and two rigid adapters for mechanical connections (Fig. 2A, fig. S1, and the "Implementation of the growable linkage" section). However, the substantial radial expansion interferes with leg movement (fig. S2A), and the axial stiffness of a growable linkage is limited to 9.5 kN/m at an internal air pressure of 14 kPa (Fig. 2B) and is prone to bursting if the air pressure is more than 14 kPa and the axial payload exceeds 105 N. Inspired by compact bones, we added a thin nonstretchable fabric cover (0.2 mm thick) on the inflatable gasbag of each growable linkage as a strain layer to increase the stiffness of the growable linkage by 16.2 times (154 kN/m under 36 kPa) and the maximum payload by 4.7 times (493 N) (details shown in the "Modeling and experiments of growable linkage" section and supplementary note 1).

Another challenge for the linkage design is that, during the growing or shrinking, the upper adapter cannot keep horizontal, which might result in the falling of the robot body above the linkage. Here, we designed a synchronous cable-constrained mechanism to connect the two adapters with four cables that are always with the

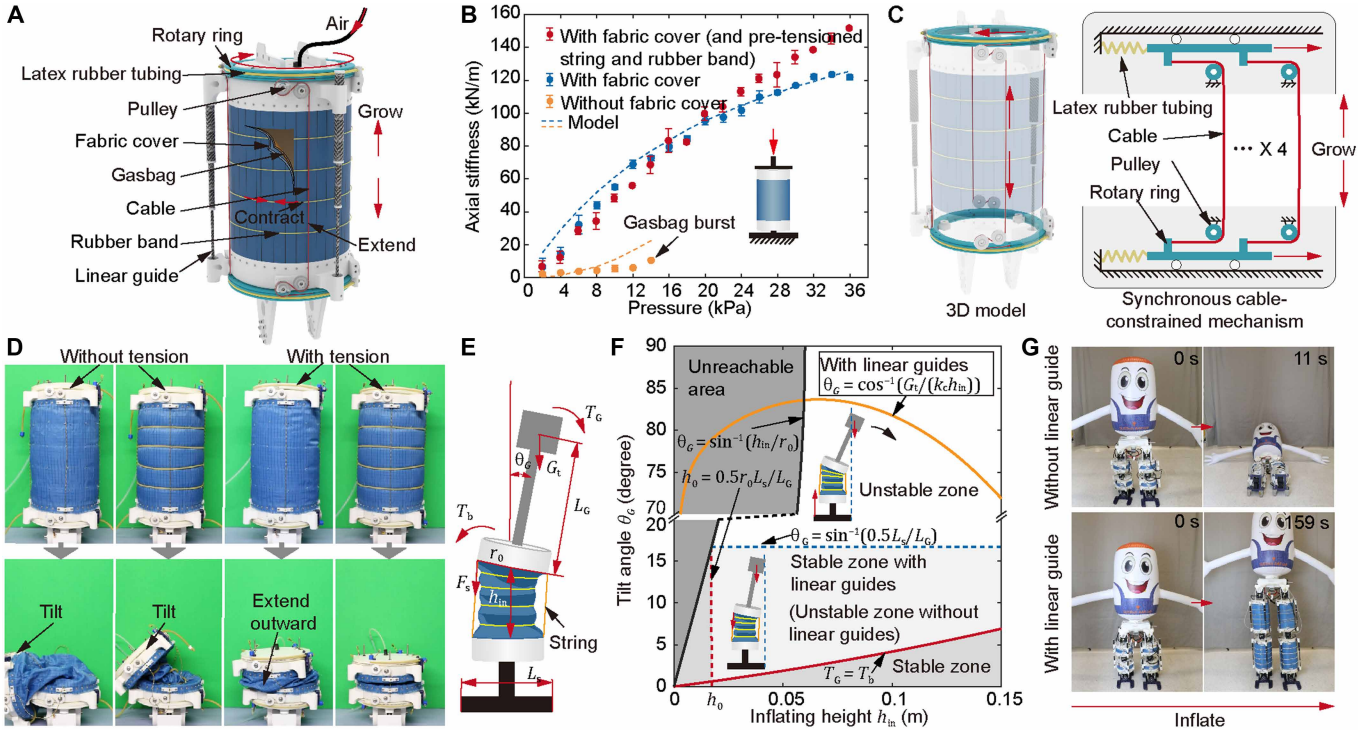

Fig. 2. The growable linkage of GrowHR. (**A**) The structure of the growable linkage. (**B**) The stiffness of the growable linkage in the axial direction under different air pressures. (**C**) The structure of the synchronous cable-constrained mechanism. (**D**) Screenshots of the deflating process of the linkages without linear guide (from left to right: without tension on cables or rubber bands; without tension on cables but with rubber bands; with tension on cables but without rubber bands; without tension on cables and rubber bands). (**E**) The force balance on the growable linkage standing vertically. (**F**) Stability analysis of the growable linkage with different tilt angles and inflating heights. (**G**) The inflating process of GrowHR without (top) and with (bottom) linear guides.

same lengths to maintain the upper and bottom adapters always parallel (Fig. 2C). During deflation, the inextensible fabric cover may become loose and extend outward from the growable linkage, potentially interfering with walking in the low-height status. To prevent this, we increased the elasticity of the fabric skin by attaching four rubber bands around the circumference to contract the cover radially during deflation (Fig. 2, A and D, and movie S1).

Moreover, the stability of the linkage under a payload is also critical. The payload on a growable linkage behaves like a weight supported by a spring-like joint because the top adapter of the linkage can tilt freely (Fig. 2E and the "Stability of the growable linkage" section). Inside of the linkage, this tilting torque from the load T_G should always equal to the balance torque T_b to avoid falling. When the inflation height of the linkage h_{in} is smaller than the adapter radius r_0, the two adapters always contact at one edge and provide a strong balance torque. Otherwise, the two adapters have no contact, and all the balance torque is provided by the cables with tension. The payload torque should be balanced with torque from the ground too, but the balance can be broken when the payload's center of mass (COM) beyond the support zone of the feet. According to the analysis (see the unstable zones in Fig. 2F), the linkage is more susceptible to falling when the height is approximately the adapter's radius. To address this, we added three custom linear guides (bending stiffness, 7.99 kN/m as h_{in} is 0 and 0.24 kN/m as $h_{in}$is 0.14 m; fig. S2B) made of carbon-fiber tubes to increase stiffness (Fig. 2A), which allows the deformation of GrowHR composed of four growable linkages while standing (Fig. 2G). With the above design, each linkage, weighing only 350 g, can change length by 315% (from 0.073 to 0.23 m) and stiffness by 960% (from 0.53 to 5.09 kN/m) (fig. S2C) to facilitate the versatility of humanoid robot.

Implementation of growable and walkable humanoid robot

Unlike previous humanoid robots that integrating rigid frames, GrowHR integrates four growable linkages that support the body as the thighs and shanks, one large gasbag that works as the deformable upper body, and one actuation flexible cable that drives the two inflatable arms to open or close simultaneously. The joints, such as ankles, knees, and hips, are driven by servomotors (fig. S4, table S1, and the "Implementation of GrowHR" section). GrowHR surpasses previous rigid humanoid robots in versatility due to its growable linkages. For example, the lightweight robot (merely 4.5 kg) can grow by 278% in height (from 0.49 m to a maximum of 1.36 m, or vice versa) by inflating the growable linkages [see comparison with humans (*25*) and previous humanoid robots (*3*, *26*–*42*) in Fig. 1C], enabling it to adapt to various applications that require different heights.

Although we demonstrated that GrowHR could shift heights while standing in the last section, walking remains challenging for the soft humanoid robot due to passive deformation of the soft growable linkages. For stability in quasistatic gait, the ground projection of GrowHR's COM should remain within the foot-support area. However, the growable linkages undergo ineligible deformation, leading to an undesirable COM drift, which increases the risk of falling or leg interference (the "Balance of GrowHR during walking" section

and supplementary note 2). During walking, the maximum deviation from the initial position of the COM (x_e) can reach up to 0.192 m (fig. S5, A and B; under 1 kPa), exceeding the balance threshold of 0.15 m, defined by the outer range of the feet. This instability increases the risk of GrowHR toppling, particularly when the robot is supported by only one foot. According to our models (the "Balance of GrowHR during walking" section), when the air pressure is large enough, the COM deviation tends to be acceptably small, and the robot is balanced (fig. S5, C and D). Thus, to minimize the effect of leg deformation, we maintained an inflation pressure above 30 kPa during walking. Additionally, we compensated for the COM deviation resulting from body deformation by adjusting the rotation angles of the servomotors (fig. S5E and the "Balance of GrowHR during walking" section). With these solutions, GrowHR achieved stable walking at full height at a speed of 11 mm/s (Fig. 3A and movie S2). In addition, we extracted the displacement of the robot's right foot during walking using an OpenCV-based visual tracking algorithm, channel and spatial reliability tracker (CSRT), discriminative correlation filter with channel and spatial reliability (*43*), and the experimental results showed reasonable agreement with the theoretical predictions (fig. S5F).

At the minimum height of GrowHR, with all air exhausted from the growable linkages, it walked at a speed of 17 mm/s (Fig. 3B). This was possible because the bending stiffness of the linear guides increased by 33.1 times (fig. S2B) compared to the fully extended state, although the legs extended freely under the force of gravity, and the feet tended to slip on the floor while walking.

The growable linkages provide GrowHR with substantial advantages in terms of portability. When fully deflated, GrowHR is compact and easy to transport. The robot can be packed into a small box

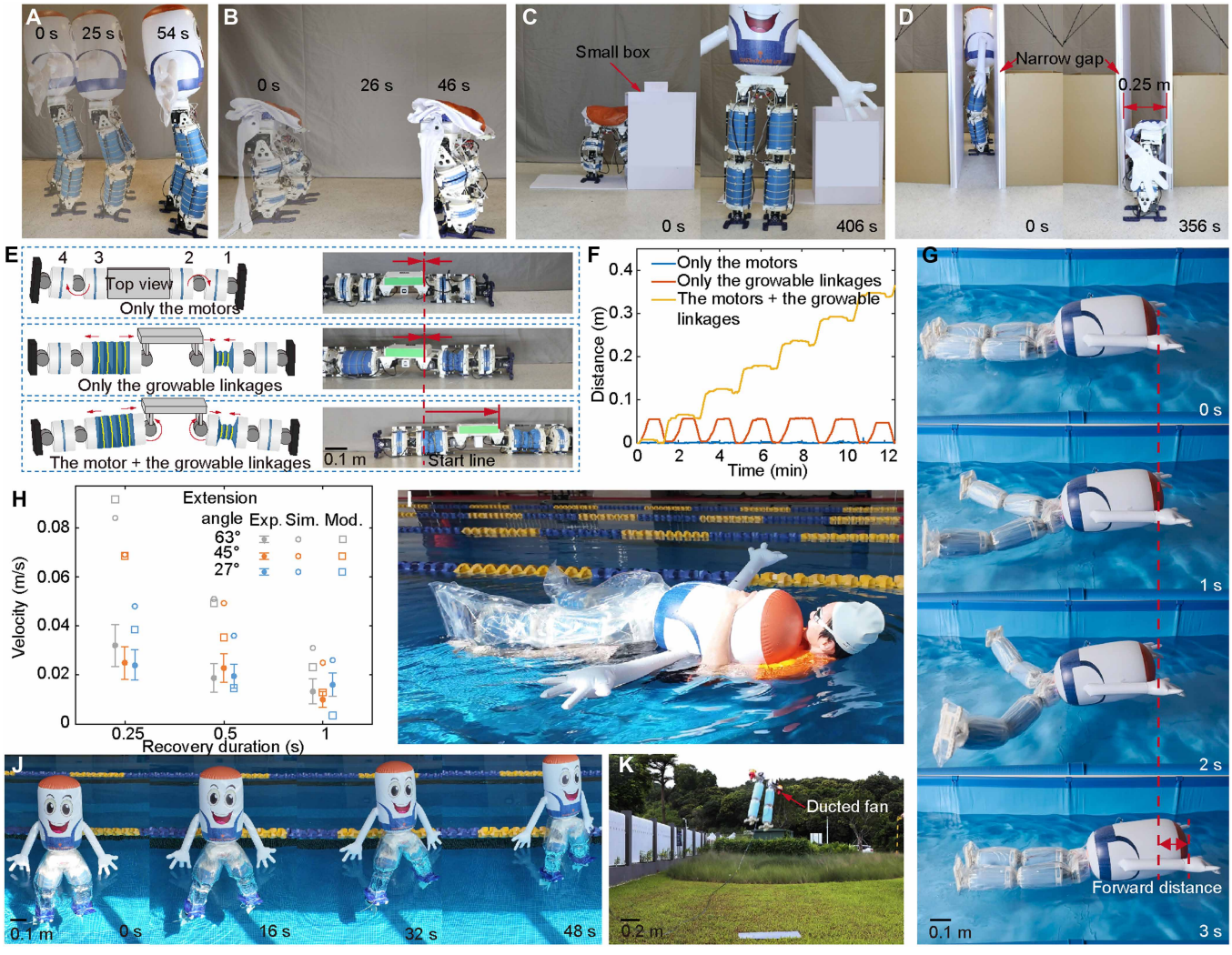

Fig. 3. Walking, crawling, swimming, and flying. (**A**) GrowHR walks at its inflated state (with the full height). (**B**) GrowHR walks at its deflated state (with the minimum height). (**C**) GrowHR walks out of a small box in the deflated state, then inflates to the full height and walks. (**D**) GrowHR walks through a narrow gap (left: GrowHR cannot fit through the gap with its initial large size; right: GrowHR successfully squeezes through the gap after deflating its body). (**E**) The crawling gait of GrowHR while it is driven by only the motors, only the growable linkages, or both the motors and the growable linkages, and the screenshots of the robot after 12.5 min of crawling. (**F**) The displacement of GrowHR with the different crawling gaits. (**G**) Screenshots of GrowHR during a swimming cycle. (**H**) Swimming velocity for different extension angles and recovery durations. A comparison between experimental, simulation and model data. (**I**) Demonstration of GrowHR saving a drowning person in a pool. (**J**) GrowHR walks on water. (**K**) GrowHR flies to the sky with two ducted fans.

(0.4 m by 0.3 m by 0.6 m) for storage or delivery (Fig. 3C and movie S3). We demonstrated that GrowHR autonomously walked out of the small box and inflated to its full height. Additionally, in our test, GrowHR deflated its upper body and legs to reduce its size to walk through a hole with a height limit of 0.55 m (40.4% of GrowHR's full height, fig. S5G and movie S3) and squeeze through a gap of merely 0.25 m (69.5% of GrowHR's full width, Fig. 3D).

Furthermore, GrowHR can perform directional turning during locomotion by adjusting the lateral inclination of its waist (supplementary note 3). By reducing the inclination toward one side, asymmetric ground friction between the feet generates a yaw moment that gradually rotates the body toward the desired direction (fig. S5, H and I). This enables smooth left or right turns without additional rotational joints, demonstrating GrowHR's capability for flexible directional walking.

Crawling with the growable linkage

Worm-inspired crawling is another innovative skill of GrowHR that the growable linkages enable. The robot can transform from walking mode to crawling mode in just 17 s by splitting its two legs (fig. S6A and movie S4). Leg splitting is a rare capability in previous humanoid robots (*44*) due to the large torque required during the transition. For instance, in our robot, the peak torque of hip motors for GrowHR (11.33 Nm) during leg splitting is more than 2.5 times higher than that in walking mode (4.47 Nm) (fig. S6, B to E, and the "Modeling and experiments of GrowHR in the crawling mode" section), exceeding the motor stall torque (8 Nm). GrowHR can split legs due to its unique capability to shrink legs by 50% and reduce the torque demand to only 50% (5.66 Nm). This allows the successful leg splitting and mode transition at the low-height state with small-power servomotors.

When the legs become in a line in opposite directions on the ground (i.e., in the crawling mode), only rotating the servomotors in a travelling wave can hardly push GrowHR to locomote forward (achieving a speed of only 0.1 mm/min in our test) due to the geometric restriction (Fig. 3, E and F; movie S5; and the "Modeling and experiments of GrowHR in the crawling mode" section). Only expanding (30-kPa air pressure) and shrinking (−30 kPa) growable linkages can neither drive GrowHR to crawl (0 mm/min on average in our test) on the ground like a worm due to the isotropic friction. GrowHR is more versatile than the previous worm-inspired robots composed of only motors or soft actuators (*45*–*47*), because it has both servomotors and growable linkages. With the cooperation of servomotors and growable linkages—the linkages expanded and shrunk while the servomotors lifted the moving parts to reduce the slipping of the ground parts (fig. S7A), GrowHR moves at a speed of 3.13 mm/min.

In addition, we developed a kinematic model for the robot's crawling process, which is used to characterize how parameters such as extendable linkage length and pressure force influence its crawling speed (fig. S7, B to E, and supplementary note 4). The results indicate that the linkage achieves its maximum extension speed at shorter lengths. Therefore, a smaller extension length leads to a higher crawling speed. Considering experimental feasibility, we selected an extension range of 46 to 66 mm for the crawling tests (fig. S7F). Furthermore, the airflow rate of the pump substantially affects crawling speed. By connecting an external air pump (with a flow rate of 2.73 liter/min), the crawling speed reached up to 1.87 mm/s, 1122 times higher than only rotating the servomotors (fig. S7, G and H) and 8.8% lower than the theoretical value (2.05 mm/s). The discrepancy between the estimated and experimental speeds is likely due to slight air leakage in the actuators, which reduced their effective extension length. Compared with other crawling robots of similar size, our robot's speed is at a lower-middle level (table S2). In future work, the crawling performance could be further improved by using pumps with higher flow rates, smaller extension lengths, and higher actuation frequencies.

Swimming and flying

The lightweight linkages with large chambers reduce the body's density of GrowHR to barely 58.2 kg/m^3 (only 5.8% of the density of the water). Thus, GrowHR can be buoyant on the water with an extra waterproof cover made of PVC film to protect the circuit and batteries (Fig. 3G). In contrast, most previous humanoid robots could not swim due to their heavy weight (more than 40 kg as the robots' height was larger than 1 m, Fig. 1C) (*33*). In our experiments, pulled by 25 kg of weight in water, approximately only half of the inflated upper body submerged (fig. S8A and movie S6). Theoretically, GrowHR can carry a load of 72.8 kg, 16.2 times heavier than its dead weight in the water, making the robot promising for applications such as transportation and rescue in water. Moreover, GrowHR can swim forward with frog kicks by driving the legs' servomotors on purpose, inspired by the breaststroke of human beings (fig. S8 and the "Modeling and experiments of GrowHR in the swimming mode" section). During swimming, larger leg extension angles and short recovery durations raise the average swimming speed (Fig. 3H and fig. S8E). The highest instantaneous swimming speed of GrowHR reached 0.27 m/s with the optimized extension angle of 63° and recovery duration of 0.25 s. In the experiments, a waterproof layer was applied to protect the electronics from liquid-induced short circuits; however, the resulting surface wrinkles likely increased hydrodynamic drag, contributing to the deviation between the experimental and simulated results. During swimming, the inflatable upper body not only enhances appearance but also adjusts body posture by lifting the front of GrowHR upward (fig. S8F). As a result, more volumes of the legs and feet are submerged, increasing swimming speed by more than 3.4 times compared to the case without the upper body (fig. S8G). We demonstrated that it approached and rescued a drowning person using its swimming capability and the strong buoyance force (Fig. 3I and movie S7). GrowHR was even able to walk on water at a speed of 16 mm/s by repeatedly extending and closing the two legs, a capability that surpasses both humans and previous humanoid robots. To maintain vertical balance, weight plates (5 kg per foot) were attached to the bottom of the feet (Fig. 3J and fig. S8, H and I), along with one-way fins, to provide directional fluid resistance.

With a total weight of only 4.5 kg, GrowHR can be easily lifted and transported through the air. To demonstrate this portability, GrowHR was carried by two ducted fans (JP 90EDF, Fig. 3K) and transported by a drone (DJI Flycart30) to a location 5.5 km away (fig. S9A and movie S8). This lightweight design enables convenient aerial transportation, making GrowHR suitable for remote applications such as search and rescue in suburban areas (fig. S9B).

The safety and versatility due to compliance of the linkage

Due to the compliant materials and structures (stretchable PVC layers and inflated chambers) of the growable soft linkages that allow energy absorption, GrowHR is intrinsically safer than previous

humanoid robots composed solely of rigid structures. In our aforementioned experiments, such as squeezing through a narrow gap (Fig. 3D) and rescuing a drowning person (Fig. 3I), GrowHR demonstrated excellent safety for its surroundings while bumping into objects and human beings. It also engaged safely with a child (as young as 6 years old) in activities such as hugging, being lifted, caught during a fall, and dragged, owing to its soft body and lightweight design (Fig. 4, A to D, and movie S9).

Beyond human safety, GrowHR's soft body also protects its internal components, particularly gearboxes and electronics, from substantial impacts. In an impact test conducted at the midpoint of the linkage using a 0.5-kg pendulum striker, the maximum acceleration, primary frequency, and energy ratio (the ratio of the kinetic energy at the measurement points after impact to the initial kinetic energy of the pendulum striker), measured at the top of the linkages, were all substantially lower in the growable linkages compared to their rigid counterparts. This indicates that the growable linkages effectively shield the electronics, gears, motors, and other components from impact damage (Fig. 4E and the "Safety test" section). Similarly, in a fall test, the maximum acceleration upon impact for the rigid counterpart was 1.74 times higher than that of GrowHR, with prolonged vibrations (Fig. 4, F and G). The rigid robot even suffered a fractured leg from the impact, whereas GrowHR's soft body remained undamaged.

Moreover, the large deformation of the growable linkages allows for a larger working space and more energy storage. For example, in a leg swing test (from 30° to 0°), the foot of the soft leg made by the growable linkages approached a point further by passive deformation than the rigid counterpart (fig. S9, C and D and movie S10). Moreover, to demonstrate the elastic properties of the soft growable linkages, the leg was deformed by an angle of up to 15.8°, which is impossible for a rigid leg, and then released while fixed to a wall. In this configuration, the leg stored elastic energy during deformation, which was rapidly released upon release, propelling a ball to a distance

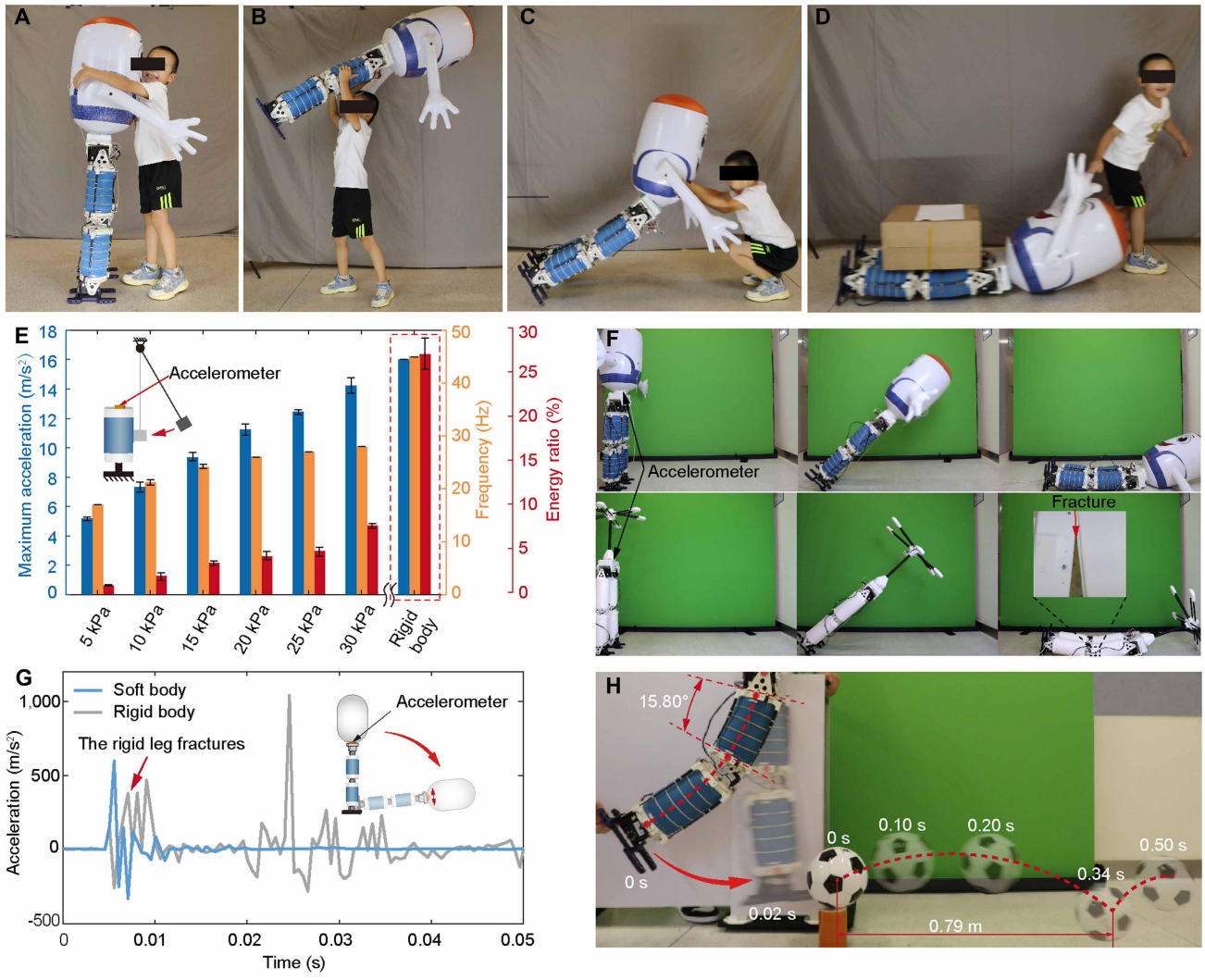

Fig. 4. GrowHR's capabilities enabled by elasticity. (**A**) GrowHR hugs a 6-year-old child safely. (**B**) Lightweight GrowHR is lifted by a child. (**C**) GrowHR falls down and collides with a child safely for both the child and the robot. (**D**) GrowHR is dragged by a child. (**E**) The maximum acceleration, primary frequency, and energy ratio of the growable linkage under different air pressures, compared with its rigid counterpart, during the pendulum strike test. (**F**) Screenshots of the fall test. (**G**) Acceleration during the fall test for GrowHR, compared with its rigid counterpart. (**H**) The leg with the growable linkages is deformed and released to kick a football.

of 0.79 m (Fig. 4H) within less than 0.02 s. This test highlights the leg's intrinsic ability to store and convert elastic energy into kinetic energy, rather than a fully autonomous kicking function of the robot.

DISCUSSION

This study presents a bioinspired design of growable linkages that are lightweight, stiff, and capable of absorbing impact, drawing inspiration from the multifunctional structure of developing human bones. These linkages are integrated into a soft humanoid robot capable of performing a diverse set of functions, some of which surpass the capabilities of traditional rigid humanoid robots, including dynamic height and shape-shifting, worm-like crawling, swimming, buoyancy control, walking on water, aerial transport with assistance, and intrinsically safe interaction with humans and the environment.

Future improvements may include increased degrees of freedom, enhanced dynamic performance through more powerful servomotors or novel actuators, and greater autonomy enabled by advanced control strategies and learning algorithms, such as large language models. This design philosophy anticipates the deployment of humanoid robots in a wide range of complex, dynamic, or hazardous environments, where they can safely and effectively perform repetitive or risky tasks alongside humans, ultimately contributing to improved safety, productivity, and quality of life.

MATERIALS AND METHODS

Implementation of the growable linkage

The core of each growable linkage on the legs is a gasbag made from PVC. A polyester fabric cover covers the gasbag to constrain radial expansion and protect the gasbag. This polyester fabric cover is connected to two three-dimensionally (3D) printed adapters at each end, limiting the growable linkage's length to a maximum of 230 mm. Four cables with tension (cable connects latex rubber tubing on both ends) also connect the two adapters (fig. S1, A and B).

As illustrated in Fig. 2C and fig. S1C, to keep the two adapters parallel, we designed a synchronous cable-constrained mechanism, which uses a closed-loop cable-pulley structure with four cables routed through fixed pulleys and connected to a rotary ring. The rotary ring is pretensioned by latex rubber tubing (4 mm diameter), which acts like a spring. When the linkage inflates and extends, the rotary ring rotates, unwinding the cables simultaneously through the pulleys. This ensures that all four cables extend by the same length, maintaining the parallel alignment between the upper and lower adapters. During contraction, the rubber tubing pulls the ring back, synchronously shortening all cables and restoring the linkage to its compact state. The linear guides further constrain the vertical motion and prevent unwanted lateral deformation or tilting. In our design, the linear guides act as passive alignment components that ensure smooth axial motion and maintain structural stability during extension and contraction. They provide necessary mechanical guidance while avoiding the complexity and weight associated with motor-driven linear actuators. Three carbon-fiber linear guides are attached to the adapters to prevent tilting or misalignment between the two adapters.

Modeling and experiments of growable linkage

We assume the growable linkage consists of two rigid adapters and a cylinder elastic membrane (fig. S2D) (*48*). The Young's modulus of the fabric cover is much larger than the inner gasbag (fig. S2, E and F), so we ignore the gasbag during calculation. According to Boyle's law and force analysis, we can obtain the relationship between the force acting on the growable linkage and its deformation (supplementary note 1). The displacement vector of the top middle point of the growable linkage can be represented by $\boldsymbol{\xi} = \Delta h\mathbf{a} + \Delta x\mathbf{r}$, where $\mathbf{a}$ and $\mathbf{r}$ are the unit vectors in the axial and the radial directions of the growable linkage, respectively, Δx denotes the deviation distance of the top middle point of the growable linkage in the radial direction, and Δh is the deviation distance in the axial direction.

We verified the above models by force-displacement experiments. The growable linkage with rubber bands and cables with tension was compressed by a tensile testing machine (MTS Criterion Model 42) through a load cell (MTS LSB.203). As estimated, the axial force increases with the displacement (fig. S2G). The stiffness in the axial direction rises with the air pressure inside the growable linkage. The larger Young's modulus of the fabric cover directly enlarges the stiffness of the growable linkage (Fig. 2B). The stiffness in the radial direction (fig. S2H) shares a similar tendency, but its magnitude is less than 5% of the axial stiffness.

Stability of the growable linkage

During the height shifting of GrowHR, even minor disturbances can result in substantial tilting and failure due to the low stiffness of its growable linkages. To simplify the analyses, a force model with a single vertical growable linkage supporting a load G_t above it is built (Fig. 2E), neglecting the linkage's own weight. Because the lower linkages in the robot are more susceptible to falling, here, we assume the linkage stands on the ground with its foot. The tilt torque induced by the load is given by $T_G = G_t L_G \sin\theta_G$, where L_G is the distance between the growable linkage and the load and θ_G is the tilt angle. For analysis, we assume the values L_G and G_t are 0.2 m and 1 kg, respectively.

When the growable linkage is not fully inflated, both the PVC gasbag layer and the fabric cover become slack and fail to provide any balance force. In such case, the only balancing torque results from the cables, calculated as $T_b = F_s r_0 \cos\theta_G$, where $F_s = k\left(h_{in} + r_0 \sin\theta_G\right)$ represents the tension force on the cable, k is the equivalent elastic coefficient of the cable caused by the latex rubber tubing, and h_{in} is the inflating height of the growable linkage. If the gravitational torque T_G exceeds this balancing torque T_b, namely, when $\theta_G \geq \tan^{-1}\left[F_s r_0 / \left(G_t L_G\right)\right]$, the load is prone to falling (fig. S3A). However, if the distance between the two adapters is less than the critical height $h_0 = 0.5 r_0 L_s / L_G$, where L_s is the supporting length of the foot, then the tilt angle is mechanically constrained $[\theta_G = \sin^{-1}\left(h_{in}/r_0\right)]$ because the two adapters lastly come into contact (fig. S3B). If the load gravity surpasses the supporting zone boundary $[\theta_G \geq \sin^{-1}\left(0.5 L_s / L_G\right)]$, then the linkage tips over, due to the torque generated by the gravity force and the supporting force from the ground (fig. S3C).

According to the above model, when the inflated height is 17 mm, the critical tilt angle is only 0.61°, which is easy to reach under a small disturbance. Therefore, we strengthen the balancing torque and the stiffness of the growable linkage to 7.99 kN/m with customized linear guides that connect the two adapters (fig. S2B). In this case, the tilt angle (fig. S3D) caused by the bending of the linear guides is calculated as $\theta_G = \tan^{-1}\left[G_t / \left(k_c h_{in}\right)\right]$, where k_c is the stiffness of the growable linkage with linear guides under 0-kPa air pressure, which is larger than 72°. By this way, GrowHR will not tip over during the height changing process, which makes it possible for the inflation and deflation of GrowHR during standing (fig. S3E).

Implementation of GrowHR

GrowHR consists of four growable linkages, one upper body, and two arms (fig. S4). The upper body structure, or head, is similar to the growable linkages but lacks a fabric cover as a constraint layer. A pair of inflatable PVC cylinders is attached to the left and right sides of the upper body to serve as arms. The growable linkages, upper body, and arms are inflated and deflated by two pumps (fspump 520-A DC 12 V) (fig. S4D), respectively, through three-way two-position solenoid valves (HIGHEND L DC 12 V).

The rigid actuators include 10 servomotors for the legs and one for the arms. Each leg is driven by five servomotors: two at the ankle (Dynamixel MX-106), one at the knee (Dynamixel MX-64), and two at the hip (Dynamixel MX-64). The two arms are driven by a servomotor (Dynamixel XL-320) located at the waist through arm actuation cables to open and close.

All growable linkages and servomotors are controlled by an onboard microcontroller (OpenCM9.04C) and powered by a lithium-polymer battery (ACE, 11.1 V, 2700 mAh). GrowHR is controlled by a remote controller (ROBOTIS RC-100) via Bluetooth.

Balance of GrowHR during walking

We adopt quasistatic gait planning to realize GrowHR walking under the inflated state. To ensure GrowHR's balance during walking, its COM must always fall in the supporting zone. The gait cycle of GrowHR is as follows. First, GrowHR shifts its COM to be above the geometric center of the supporting foot by tilting its body. It then lifts the other foot and moves forward. Afterward, GrowHR adjusts the angles of its joints to move its weight forward while keeping both feet in contact with the ground.

To build the balance model, first, we regard GrowHR as a rigid biped robot with 10 degrees of freedom (the upper body and arms are neglected) and ignore the deformation of the growable linkage. On the basis of the Denavit-Hartenberg parameters and coordinate system (fig. S4B and table S3) (*49*), we can achieve the transformation matrices for the joints and calculate the position of each mass point (fig. S4E). The details shown in supplementary note 2.

Then, we can add the effect of deformation into the above model. When the robot is supported solely by its right foot, the deformation of each growable linkage influences the robot's overall COM. According to the "Modeling and experiments of growable linkage" section, the displacement vector, $\boldsymbol{\xi}_j$, of the jth growable linkage due to the deformation is determined by the internal air pressure and the cumulative force applied at its free end. On the basis of the displacement vector, the deviation of the COM from its initial standing position along the y axis x_e can be calculated (supplementary note 2).

According to these models, we can analyze the position of the robot COM and x_e during the walking process (fig. S5, C and D). With larger air pressure inside the growable linkages, GrowHR becomes more rigid, and the maximum x_e drops. In this work, the balance threshold for the maximum x_e is 0.15 m, corresponding to the outer edges of the footprints. If x_{COM} is 0.09 m and the air pressure is 1 kPa, then the large maximum deviation makes the projection of the COM out of the footprint, and GrowHR tends to fall. However, if the air pressure is larger than 2.3 kPa, then the projection of the COM is always inside the supporting zone, although a little deformation occurs on the growable linkages. Thus, this study inflates GrowHR with 30 kPa for balance during walking.

Except for inflating with higher air pressure, we also compensate for the deviation resulting from deformation by rotating the servomotors with a compensated angle to prevent GrowHR from falling and avoid interference between the two legs during walking due to the deformation of the moving leg. The compensate angle $\alpha \approx \sin^{-1}\left(\Delta x'/L_0\right)$ can be obtained by $\Delta x'$ (the projection of the deformation Δx into the normal plane of the rotation joint) and L_0 (the inflated length of the growable linkage) (fig. S5E).

Modeling and experiments of GrowHR in the crawling mode

When GrowHR transits from the walking mode to the crawling mode (fig. S6, C to E), the torque required on the hip motor is τ_{split}. Based on the model in supplementary note 4, the motor at the hip joint needs to provide higher torque as the body is up (11.33 Nm at maximum) or down (10.51 Nm at maximum). These requirements on the motor torque exceed the stall torque of the motors (8 Nm) and the torque τ_{walk} requirements on the hip motor (fig. S6B) during walking (4.47 Nm at maximum). That is also why, previously, splitting and transition between standing and crawling of humanoid robots were merely reported. For GrowHR, this challenge can be circumvented by simply reducing the length of the legs by deflating. The maximum torque requirements are reduced to only 50% (5.66 Nm up and 5.25 Nm down at maximum, respectively) if the leg's length is reduced by 50%.

When only the motors are active in the crawling mode, achieving a snake-like motion along the length is straightforward as the joint motors move in a sequential rotation. The speed is $v_c = A\sin^2(\gamma/2)$, where A is the coefficient and γ is the maximum bending angle of the joint (*50*).

When GrowHR lying on the ground travels like a worm only by expansion and shrinkage of the growable linkages, ideally, the speed is $v_c = d_c / T_c$, where d_c is the expansion distance of a growable linkage in one robot locomotion cycle T_c. GrowHR is subjected to two external forces: the friction force of the static part and that of the moving parts acting in opposite directions. Typically, the lighter part is driven to move, while the heavier part remains stationary, as its greater static friction prevents displacement. In GrowHR, the waist section (which includes batteries, pumps, motors, and electronics) accounts for more than 40% of the total weight, making it nearly as heavy as the remaining components. Consequently, moving the waist induces substantial slippage in other parts, causing the robot to oscillate forward and backward with a negligible net displacement.

When the growable linkages and the motors cooperate, the situation changes (fig. S7A). First, link 1 and link 4 are lifted off the ground by rotating the motors at the hip joints, while link 2 inflates to push link 1 forward, and link 3 deflates to pull link 4 forward. Then, the hip motors rotate opposite to press link 1 and link 4 on the ground but elevate the waist part. Following this, link 2 deflates, and link 3 inflates, pulling the waist forward. This coordinated sequence reduces friction in the moving parts as the lifting force from the motors decreases the normal force, thereby reducing frictional resistance of the lifting part, preventing slippage of the stationary parts. Using this method, GrowHR achieves its highest speed, outperforming locomotion strategies that use only motors or growable linkages independently.

Modeling and experiments of GrowHR in the swimming mode

To test the buoyance force of GrowHR, we mainly tested the inflated upper body's buoyance force because the whole body's buoyance force was too large (72.8 kg) according to our calculation. In the

experiment, we tied weights to the upper body by a cotton rope net. With more than 25 kg weight, only half of the upper body was submerged in the water (fig. S8A).

Inspired by breaststroke swimming of humans, the robot's legs started in a straight and closed position. They then extended and bent at the knees, before lastly recovering to push the body forward in the water and straightening the knees (fig. S8B). The swimming speed is decided by the leg extension and recovering speed according to the Morison equation (supplementary note 5) (*51*). According to this model, the swimming speed directly depends on the extension angle, the recovery duration of the legs, the leg's cross-section area submerged in water, and the immersion depth of the leg in the water. Theoretical analysis and simulations using the Swumsuit simulator (*52*, *53*) show close agreement, and both predict trends consistent with experimental observations (Fig. 3H and fig. S8, C and D). Specifically, increasing the extension angle and reducing the recovery duration are predicted to substantially enhance the swimming speed, which aligns with what we observed experimentally (Fig. 3H and fig. S8E). Thus, we improve the swimming speed of GrowHR by enlarging the extension angle and shortening the recovery duration. Overall, the theory, simulation, and experiments exhibit similar trends, confirming the validity of our approach. GrowHR without the upper body swims not as quickly as the one with the upper body (fig. S8, F and G). This phenomenon occurs because the buoyancy force acting on the upper body generates a torque that helps submerge more of the legs and feet, thereby increasing the propulsive force. Future enhancements in the swimming strategy could be achieved by developing more advanced algorithms.

The swimming experiments were conducted in a swimming pool. GrowHR was waterproofed by warping transparent PVC (thickness, 0.5 mm) film. The edge of the film was sealed by an impulse portable sealing machine (power, 600 W; sealing width, 5 mm; and sealing time, 5 s). In the robotic rescue demonstration, the remote-controlled GrowHR swam to the drowning person (Fig. 3I) and carried him to the pool's edge. A trained volunteer acted as the drowning person, and the experiment was conducted under controlled and safe conditions.

Moreover, GrowHR stood and walked on water using weights (5 kg for each foot) and customized fins on the foot (fig. S8, H and I). The fins opened, generating high resistance when the feet moved backward. They closed as the feet moved forward, enabling one-directional propulsion during GrowHR's leg extension and recovery. We used the slider-crank mechanism to make sure the two fins moved symmetrically. Nylon cable ties attach the customized fin to GrowHR's foot.

Safety test

In the impact test, the pendulum striker (0.5 kg) was hanged by a rod of 0.5 m. Initially, the pendulum striker started from the position that the angle between the rod and the vertical plane was 30° (Fig. 4E).

In the fall test, we installed an accelerometer (WIT, ADXL375) at the waist of GrowHR to record its acceleration (Fig. 4, F and G). At the beginning of the experiment, GrowHR stood upright, and, then, it was pushed to fall (the initial acceleration can be negligible). The rigid counterpart was constructed by substituting the growable linkages with 3D printed rigid components and replacing the upper body with a truss structure composed of carbon-fiber tubes. The experimental results showed that the acceleration impact (599 m/s^2) of GrowHR is 42.5% less than that of the rigid robot (1041 m/s^2).

We demonstrated the compliance of the leg by a swing test (fig. S9C and movie S10). One leg of GrowHR was fixed on the hip joint, and the internal air pressure of the growable linkages was 0 kPa. The leg at initial angle 30° swung downward with the hip joint motor until the leg returned to the 0° position. After stopped by the hip joint motor, the soft leg was deformed and continued to swing due to the inertia, while the rigid counterpart stopped because of the geometric constraint. The results indicate that the soft leg generates a larger displacement at the x direction (161 mm, the red marker point at the foot, fig. S9C) due to the elasticity of the growable linkages compared with the rigid leg (129 mm) (fig. S9D), along with a longer decay time.

AI-assisted manuscript preparation

In preparing parts of the manuscript, the authors used the artificial intelligence (AI)–assisted large language model ChatGPT (OpenAI, version 4o). ChatGPT was provided with specific prompts such as "Polish scientific writing for clarity and conciseness" and "Improve the readability of this paragraph while maintaining technical accuracy." All outputs generated by ChatGPT were carefully reviewed, edited, and verified by the authors to ensure accuracy, originality, and the absence of bias or plagiarism. ChatGPT was used solely as an assistive tool for improving the clarity and readability of the manuscript, while all scientific content, data analysis, and interpretations were independently performed and verified by the authors.

Supplementary Materials

The PDF file includes:

Supplementary Notes 1 to 5
Figs. S1 to S9
Tables S1 to S3
Legend for movies S1 to S10
References

Other Supplementary Material for this manuscript includes the following:

Movies S1 to S10

REFERENCES

1. S. Kajita, H. Hirukawa, K. Harada, K. Yokoi, *Introduction to Humanoid Robotics* (Springer, 2014), vol. 101.
2. G. Ficht, S. Behnke, Bipedal humanoid hardware design: A technology review. *Curr. Robot. Rep.* **2**, 201–210 (2021).
3. R. Bogue, Humanoid robots from the past to the present. *Ind. Robot.* **47**, 465–472 (2020).
4. P. Slade, C. Atkeson, J. M. Donelan, H. Houdijk, K. A. Ingraham, M. Kim, K. Kong, K. L. Poggensee, R. Riener, M. Steinert, On human-in-the-loop optimization of human–robot interaction. *Nature* **633**, 779–788 (2024).
5. S. Saeedvand, M. Jafari, H. S. Aghdasi, J. Baltes, A comprehensive survey on humanoid robot development. *Knowl. Eng. Rev.* **34**, e20 (2019).
6. A. Zacharaki, I. Kostavelis, A. Gasteratos, I. Dokas, Safety bounds in human robot interaction: A survey. *Saf. Sci.* **127**, 104667 (2020).
7. S. Mukherjee, M. M. Baral, S. K. Pal, V. Chittipaka, R. Roy, K. Alam, in *2022 International Conference on Machine Learning, Big Data, Cloud and Parallel Computing (COM-IT-CON)* (IEEE, 2022), vol. 1, pp. 822–826.
8. M. Kyrarini, F. Lygerakis, A. Rajavenkatanarayanan, C. Sevastopoulos, H. R. Nambiappan, K. K. Chaitanya, A. R. Babu, J. Mathew, F. Makedon, A survey of robots in healthcare. *Technologies* **9**, 8 (2021).
9. V. Villani, F. Pini, F. Leali, C. Secchi, Survey on human–robot collaboration in industrial settings: Safety, intuitive interfaces and applications. *Mechatronics* **55**, 248–266 (2018).
10. M. Del Giudice, V. Scuotto, L. V. Ballestra, M. Pironti, Humanoid robot adoption and labour productivity: A perspective on ambidextrous product innovation routines. *Int. J. Hum. Resour. Manag.* **33**, 1098–1124 (2022).
11. J. S. Mehling, P. Strawser, L. Bridgwater, W. K. Verdeyen, R. Rovekamp, in *Proceedings 2007 IEEE International Conference on Robotics and Automation* (IEEE, 2007), pp. 2928–2933.
12. K. Darvish, L. Penco, J. Ramos, R. Cisneros, J. Pratt, E. Yoshida, S. Ivaldi, D. Pucci, Teleoperation of humanoid robots: A survey. *IEEE Trans. Robot.* **39**, 1706–1727 (2023).

13. Q. Zhang, C. Zhao, L. Fan, Y. Zhang, Taikobot: A full-size and free-flying humanoid robot for intravehicular astronaut assistance and spacecraft housekeeping. *Machines* **10**, 933 (2022).
14. M. A. Diftler, J. S. Mehling, M. E. Abdallah, N. A. Radford, L. B. Bridgwater, A. M. Sanders, R. S. Askew, D. M. Linn, J. D. Yamokoski, F. Permenter, in *2011 IEEE International Conference on Robotics and Automation* (IEEE, 2011), pp. 2178–2183.
15. B. Choi, W. Lee, G. Park, Y. Lee, J. Min, S. Hong, Development and control of a military rescue robot for casualty extraction task. *J. Field Robot.* **36**, 656–676 (2019).
16. K. Kim, P. Spieler, E.-S. Lupu, A. Ramezani, S.-J. Chung, A bipedal walking robot that can fly, slackline, and skateboard. *Sci. Robot.* **6**, eabf8136 (2021).
17. M. DeDonato, V. Dimitrov, R. Du, R. Giovacchini, K. Knoedler, X. Long, F. Polido, M. A. Gennert, T. Padır, S. Feng, Human-in-the-loop control of a humanoid robot for disaster response: A report from the DARPA robotics challenge trials. *J. Field Robot.* **32**, 275–292 (2015).
18. R. Setiawati, P. Rahardjo, "Bone development and growth," in *Osteogenesis and Bone Regeneration* (Books on Demand, 2019), vol. 10, pp. 82452.
19. B. Mazzolai, F. Tramacere, I. Fiorello, L. Margheri, The bio-engineering approach for plant investigations and growing robots. A mini-review. *Front. Robot. AI* **7**, 573014 (2020).
20. E. Del Dottore, A. Sadeghi, A. Mondini, V. Mattoli, B. Mazzolai, Toward growing robots: A historical evolution from cellular to plant-inspired robotics. *Front. Robot. AI* **5**, 16 (2018).
21. E. Del Dottore, A. Mondini, N. Rowe, B. Mazzolai, A growing soft robot with climbing plant–inspired adaptive behaviors for navigation in unstructured environments. *Sci. Robot.* **9**, eadi5908 (2024).
22. S. Al Harthy, H. Sadati, C. Girerd, S. Kim, Z. Wu, B. Saldarriaga, C. Seneci, T. Morimoto, C. Bergeles, Tip-growing robots: Design, theory, application. *IEEE Trans. Robot.* **41**, 5511–5532 (2024).
23. Y. Shan, Y. Zhao, H. Wang, L. Dong, C. Pei, Z. Jin, Y. Sun, T. Liu, Variable stiffness soft robotic gripper: Design, development, and prospects. *Bioinspir. Biomim.* **19**, 011001 (2023).
24. M. E. Giannaccini, C. Xiang, A. Atyabi, T. Theodoridis, S. Nefti-Meziani, S. Davis, Novel design of a soft lightweight pneumatic continuum robot arm with decoupled variable stiffness and positioning. *Soft robotics* **5**, 54–70 (2018).
25. S. v. Buuren, Y. Schönbeck, P. v. Dommelen, "Collection, collation and analysis of data in relation to reference heights and reference weights for female and male children and adolescents (0-18 years) in the EU, as well as in relation to the age of onset of puberty and the age at which different stages of puberty are reached in adolescents in the EU" (EFSA Supporting Publications 9, 255E, 2012).
26. P. Allgeuer, H. Farazi, M. Schreiber, S. Behnke, in *2015 IEEE-RAS 15th International Conference on Humanoid Robots (Humanoids)* (IEEE, 2015), pp. 33–40.
27. I. I. Álvarez, "Xiaomi presenta CyberOne, su primer robot humanoide," *Computerworld Spain*, 16 August 2022.
28. J. Englsberger, A. Werner, C. Ott, B. Henze, M. A. Roa, G. Garofalo, R. Burger, A. Beyer, O. Eiberger, K. Schmid, in *2014 IEEE-RAS International Conference on Humanoid Robots* (IEEE, 2014), pp. 916–923.
29. G. Ficht, P. Allgeuer, H. Farazi, S. Behnke, in *2017 IEEE-RAS 17th International Conference on Humanoid Robotics (Humanoids)* (IEEE, 2017), pp. 669–675.
30. J. Jeong, J. Yang, G. H. G. Christmann, J. Baltes, Lightweight mechatronic system for humanoid robot. *Knowl. Eng. Rev.* **38**, e5 (2023).
31. T. Jung, J. Lim, H. Bae, K. K. Lee, H.-M. Joe, J.-H. Oh, Development of the humanoid disaster response platform DRC-HUBO+. *IEEE Trans. Robot.* **34**, 1–17 (2018).
32. K. Kaneko, H. Kaminaga, T. Sakaguchi, S. Kajita, M. Morisawa, I. Kumagai, F. Kanehiro, Humanoid robot HRP-5P: An electrically actuated humanoid robot with high-power and wide-range joints. *IEEE Robot. Autom. Lett.* **4**, 1431–1438 (2019).
33. F. R. Noreils, Humanoid Robots at work: Where are we? arXiv:2404.04249 (2024).
34. S. Saeedvand, H. S. Aghdasi, J. Baltes, Novel lightweight odometric learning method for humanoid robot localization. *Mechatronics* **55**, 38–53 (2018).
35. Y. Sakagami, R. Watanabe, C. Aoyama, S. Matsunaga, N. Higaki, K. Fujimura, in *IEEE/RSJ International Conference on Intelligent Robots and Systems* (IEEE, 2002), vol. 3, pp. 2478–2483.
36. O. Stasse, T. Flayols, R. Budhiraja, K. Giraud-Esclasse, J. Carpentier, J. Mirabel, A. Del Prete, P. Souères, N. Mansard, F. Lamiraux, in *2017 IEEE-RAS 17th International Conference on Humanoid Robotics (Humanoids)* (IEEE, 2017), pp. 689–695.
37. R. K. Nichols, C. M. Carter, J. V. Drew II, M. Farcot, C. J.-P. Hood, M. J. Jackson, P. D. Johnson, S. Joseph, S. Kahn, W. D. Lonstein, *Cyber-Human Systems, Space Technologies, and Threats* (Artificial Brains and Body, 2023).
38. H. Ding, Z. Shi, Y. Hu, J. Li, B. Yu, P. Zhang, Lightweight design optimization for legs of bipedal humanoid robot. *Structural and Multidisciplinary Optimization* **64**, 2749–2762 (2021).
39. T. Seo, S. Ryu, J. H. Won, Y. Kim, H. S. Kim, Stair-climbing robots: A review on mechanism, sensing, and performance evaluation. *IEEE Access* **11**, 60539–60561 (2023).
40. A. A. Malik, T. Masood, A. Brem, in *Companion of the 2024 ACM/IEEE International Conference on Human-Robot Interaction* (ACM/IEEE, 2024), pp. 20–27.
41. E. Ackerman, Year of the Humanoid: Legged robots from eight companies vie for jobs. *IEEE Spectrum* **61**, 44–48 (2024).
42. Y. Liang, F. Yin, Z. Li, Z. Xiong, Z. Peng, Y. Zhao, W. Yan, Reduced-dimensional whole-body control based on model simplification for bipedal robots with parallel mechanisms. *IEEE Robot. Autom. Lett.* **10**, 1696–1703 (2025).
43. K. Farkhodov, S.-H. Lee, K.-R. Kwon, in *Bioimaging* (SciTePress, 2020), pp. 209–212.
44. R. Thakker, A. Kamat, S. Bharambe, S. Chiddarwar, K. M. Bhurchandi, in *2014 IEEE/RSJ International Conference on Intelligent Robots and Systems* (IEEE, 2014), pp. 309–314.
45. Z. J. Tang, J. Q. Lu, Z. Wang, W. W. Chen, H. Feng, Design of a new air pressure perception multi-cavity pneumatic-driven earthworm-like soft robot. *Auton Robots* **44**, 267–279 (2020).
46. C. Jiang, Z. G. Pei, An in-pipe worm robot with pneumatic actuators based on origami paper-fabric composites. *Text. Res. J.* **91**, 2724–2737 (2021).
47. J. D. Liu, Y. C. Tong, J. G. Liu, Review of snake robots in constrained environments. *Robot. Auton. Syst.* **141**, 103785 (2021).
48. J.-J. Chen, Z.-H. Yin, S. Rakheja, J.-H. He, K.-H. Guo, Theoretical modelling and experimental analysis of the vertical stiffness of a convoluted air spring including the effect of the stiffness of the bellows. *Proc. Inst. Mech. Eng. D.* **232**, 547–561 (2018).
49. H. Lipkin, in *International Design Engineering Technical Conferences and Computers and Information in Engineering Conference* (American Society of Mechanical Engineers, 2005), vol. 47446, pp. 921–926.
50. F. L. Chernousko, Modelling of snake-like locomotion. *Appl. Math Comput.* **164**, 415–434 (2005).
51. Y. Yi, Z. Jianqing, X. Han, C. Maokuan, Z. Lu, Z. Zhongjing, in *2016 IEEE International Conference on Advanced Intelligent Mechatronics (AIM)* (IEEE, 2016), pp. 633–638.
52. M. Nakashima, in *Proceedings of the 2005 International Symposium on Computer Simulation in Biomechanics (ISCSB2005)* (Curran Associates Inc. 2005), vol. 7, pp. 65–66.
53. M. Nakashima, K. Satou, Y. Miura, Development of swimming human simulation model considering rigid body dynamics and unsteady fluid force for whole body. *J. Fluid Sci. Technol.* **2**, 56–67 (2007).
54. Z. Zhang, X. Wang, S. Wang, D. Meng, B. Liang, Design and modeling of a parallel-pipe-crawling pneumatic soft robot. *IEEE Access* **7**, 134301–134317 (2019).
55. J. Zou, Y. Lin, C. Ji, H. Yang, A reconfigurable omnidirectional soft robot based on caterpillar locomotion. *Soft Robot.* **5**, 164–174 (2018).
56. Z. G. Joey, A. A. Calderón, N. O. Pérez-Arancibia, in *2017 IEEE international conference on robotics and biomimetics (ROBIO)* (IEEE, 2017), pp. 834–841.
57. J. Liu, P. Li, Z. Huang, H. Liu, T. Huang, Earthworm-Inspired multimodal pneumatic continuous soft robot enhanced by winding transmission. *Cyborg Bionic Syst.* **6**, 0204 (2025).
58. R. Das, S. P. M. Babu, F. Visentin, S. Palagi, B. Mazzolai, An earthworm-like modular soft robot for locomotion in multi-terrain environments. *Sci. Rep.* **13**, 1571 (2023).
59. M. Lopez, M. Haghshenas-Jaryani, A study of energy-efficient and optimal locomotion in a pneumatic artificial muscle-driven snake robot. *Robotics* **12**, 89 (2023).
60. B. Seyidoğlu, A. Rafsanjani, A textile origami snake robot for rectilinear locomotion. *Device* **2**, 100226 (2024).
61. Y. Zhao, H. Huang, W. Yuan, X. Liu, C. C. Cao, Worm-inspired, untethered, soft crawling robots for pipe inspections. *Soft Robot.* **11**, 639–649 (2024).
62. X. Qi, T. Gao, X. Tan, Bioinspired 3D-printed snakeskins enable effective serpentine locomotion of a soft robotic snake. *Soft Robot.* **10**, 568–579 (2023).
63. M. Li, G. Wang, J. Wang, Y. Zheng, X. Jiao, Development of an inchworm-like soft pipe robot for detection. *Int. J. Mech. Sci.* **253**, 108392 (2023).

Acknowledgments: In preparing parts of the manuscript, we used the AI-assisted large language model ChatGPT (OpenAI, version 4o). All outputs were carefully checked and edited by the authors to ensure accuracy, originality, and the absence of bias or plagiarism. **Funding:** This work was supported by the Natural Science Foundation of China under grants 52450323 (H.W.) and 52275021 (H.W.), Natural Science Foundation of Guangdong Province of China under grant 2024A1515010183 (H.W.), and Guangdong Provincial Research Support Program under grant 2019QN01Z733 (H.W.). **Author contributions:** H.W., H.L., and Y.Y. proposed and designed the research. H.L., Y.Y., and J.Y. built the robot. H.L., Y.Y., and J.Y. conducted the experimental work. H.L. and H.W. contributed to modeling and data analysis. H.L., T.W., and H.W. wrote the paper. All authors provided feedback. **Competing interests:** H.W. and H.L. are coinventors on a pending patent application filed by the China National Intellectual Property Administration (application no. 2024108667801; filed 1 July 2024) related to this work. The authors declare that they have no other competing interests. **Data and materials availability:** All data and code needed to evaluate and reproduce the results in the paper are present in the paper and/or the Supplementary Materials.

Submitted 3 July 2025
Accepted 22 December 2025
Published 23 January 2026
10.1126/sciadv.aea2831